Article:
Song, B, Hua, Y, Zhou, C et al. (3 more authors) (2022) Fabrication and anticorrosion behavior of a bi-phase TaNbHfZr/CoCrNi multilayer coating through magnetron sputtering. Corrosion Science, 196. 110020. ISSN 0010-938X

https://doi.org/10.1016/j.corsci.2021.110020

Fabrication and anticorrosion behavior of a bi-phase TaNbHfZr/CoCrNi multilayer coating through magnetron sputtering

Baorui Song[1,3], Yong Hua[*2], Chaozheng Zhou[1], Yanhuai Li[1], Liuquan Yang[3], Zhongxiao Song[*1]

1: State Key Laboratory for Mechanical Behavior of Materials, Xi'an Jiaotong University, Xi'an 710049, Shaanxi, P.R. China.

Email: zhongxiaosong@mail.xjtu.edu.cn

2: Corrosion and Integrity Centre, Zhejiang JIULI Hi-Tech Metals Co. Ltd, Hu Zhou, P.R. China.

Email: leo.huayong@gmail.com

3: Institute of Functional Surfaces, School of Mechanical Engineering, University of Leeds, Leeds LS2 9JT, United Kingdom

*: Authors to whom correspondence should be addressed.

Keywords: high entropy alloy, multilayer coating, magnetron sputtering, corrosion properties

Abstract

A novel multilayer coating containing bi-phase structures was designed via a magnetron sputtering method. Surface morphologies, phase structure and corrosion behavior of TaNbHfZr/CoCrNi coating have been investigated via a combination of electrochemistry and surface analysis. Such bi-phase structures containing fcc CoCrNi and amorphous TaNbHfZr layers exhibited an improved corrosion resistance compared with CoCrNi monolayer coating. The hardness and elastic modulus of the TaNbHfZr/CoCrNi multilayer coating were slightly lower than the CoCrNi monolayer coating due to the softening induced by the amorphous TaNbHfZr layer, revealing that such multilayer structure possesses the desired corrosion performance and maintains good mechanical properties.

Keywords: Coating; Corrosion; HEAs; MEAs; magnetron sputtering

1. Introduction

The high entropy alloys (HEAs) with simple microstructure but complex stoichiometry were firstly defined by Yeh et al. in 2004 [1]. The definition of HEAs composes of five or more metal elements such as Cr, Co, Fe, Mo, etc., with the concentration of each element in the range of 5~35 at.% [1]. In recent years, researchers have reported on the exploration of various HEAs or medium entropy alloys (MEAs) with superior properties such as excellent corrosion resistance [2, 3], high strength or hardness [4] and high stability [5]. It is imperative to open the pathway for a broader practical application, especially in the structural field and long-term engineering applications requiring an outstanding combination of both mechanical and corrosion performance. The “cocktail effect” was considered for HEAs/MEAs to integrate functional elements into a different and specific utilization [6, 7]. The incorporation of passivating elements Cr, Ni, Co, Mo, etc. can enhance the corrosion resistance, the addition of refractory Ta, Nb, Cr, etc. can improve the mechanical performance or the stability in extreme environments [8]. As reported in our previous work, the hardness of the TaNbHfZr amorphous coating reaches ~8 GPa [9]. Shi et al. [10] have reported that CoCrNi MEA with face-centered cubic (fcc) structure has excellent strength and toughness as well as corrosion resistance, which are considered as the basic components for the promising engineering alloys demanding in the extreme and highly-sensitive engineering service environments. Wang et al. [11] compared bulk CoCrNi MEA with 304 (SS), the results found that CoCrNi exhibited superior corrosion resistance in a 1 M H_2SO_4 solution and Co oxides were found as the main constituents within the passive film.

The conventional approaches to fabricate HEAs/MEAs are mainly by arc melting or casting with high cost due to the complicated fabrication processes [12]. It has been reported that the HEA/MEA coatings which are compositionally the same as the bulk material manufactured via conventional approach, while possessing better corrosion-resistant properties [13], also nearly twice the hardness compared to that of bulk materials [14, 15]. Feng et al. [12] reported that the laser cladded CoCrNi coating possessed a more positive passive potential in a 0.5 M H_2SO_4 solution.

Recently, a growing number of investigations have been focused on HEA/MEA coatings. Magnetron sputtering (MS), as one of the physical vapor deposition (PVD) methods, has been widely used to fabricate coatings in aerospace [16-18], automotive [19], cutting tools [20] and watches [21], etc. Comparatively, MS possesses the “rapid quenching effect” with a fast cooling rate which can restrict the diffusion of elements and thus restrain the nucleation and growth of intermetallic compounds, in favor of the formation of HEA/MEA solid-solution [22, 23], therefore, more homogeneous, dense microstructure and uniform compositional distribution can be obtained in the HEA/MEA coatings via MS methods [24] and also the use of MS to fabricate HEA/MEA coating is more environmentally friendly than traditional melting or casting approaches [25]. However, in the monolayer coating, the columnar structure and defects such as voids, pinholes, pores or cracks can lead to open paths between the substrate and the corrosive environment [26, 27].

Structural design of HEA/MEA coatings can be optimized for stability and corrosion resistance, the mixing entropy contributes to the formation of solid solutions with fcc, body-centered cubic (bcc), hexagonal closest packed (hcp), or amorphous structure. The high mixing entropy enhances the mutual solubility of various elements and prevents phase segregation, meanwhile, the large atomic size difference causes severe lattice distortion and favors the amorphous structure due to the local elastic strain [28]. It has been reported that the amorphous structure is beneficial to the corrosion resistance of the functional coatings due to the absence of grain boundary than the corresponding crystalline structure [22]. Therefore, a simple and robust strategy to combine HEA/MEA with amorphous structures in a multilayer coating with harder and better corrosion resistance is still necessary to enable its practical application. The multilayer structure can effectively reduce stress concentration [29], and large number of interfaces can block the growth of coarse columnar grain making the coating more compact [30], preventing the propagation of cracks or pores and improving the overall performance.

Herein, an innovative strategy via PVD methodology was implemented to fabricate a functionally anticorrosive multilayer coating. The corrosion resistance was

substantially improved by a multilayer coating combining CoCrNi MEA with TaNbHfZr high entropy metallic glass layers, which also retains the mechanical performance at a good level. The corrosion behavior and mechanical properties of the developed coatings were investigated by a series of surface analysis, nanoindentation and electrochemical tests.

2. Experimental

2.1 Material manufacture via PVD methods

The multilayer TaNbHfZr/CoCrNi coating was prepared by DC magnetron sputtering using equiatomic CoCrNi ternary and quaternary TaNbHfZr targets (Φ 75 mm ×5 mm), which were made via powder metallurgy with purities >99.99 %. For comparison, a monolayer CoCrNi or TaNbHfZr coating with the same thickness was also prepared. P-type (100) Si wafers and 304 SS were chosen as substrates for microstructural characterization and electrochemical tests, respectively. The base pressure prior to the deposition was less than 5×10^{-4} Pa. Prior to deposition, the surface of 304 SS was ground up to 3000 # SiC papers, followed by mirror finishing via the diamond polishing spray on a flannel cloth to reduce the surface roughness (Ra~3 nm), and then cleaned ultrasonically using acetone and alcohol for 15 mins. During deposition, Ar flow rate was kept at 30 sccm and the working pressure was 0.45 Pa; the bias was set as -70 V, which is optimized to ensure good adhesion between the coatings and the substrates; the DC powers were 150 W and 120 W for TaNbHfZr layer and CoCrNi layer, respectively. Each CoCrNi or TaNbHfZr layer was deposited in sequence to form the multilayer TaNbHfZr/CoCrNi coating and the whole deposition process of the multilayer was continuous layer by layer in a vacuum environment thus the multilayer was an integrated coating, and the thickness of each layer was controlled by the deposition time.

2.2 Surface analysis

The phase structure was characterized by an x-ray diffractometer (XRD) with Cu Kα radiation on a Bruker D8 Discover powder x-ray diffractometer. High-resolution transmission electron microscopy (HRTEM, JEM-2100F) experiments were performed

to investigate the cross-sectional microstructure. Scanning electron microscopy (SEM, FEI-VERIOS460) with EDS (Energy Dispersive Spectrometer) was employed to observe the top surface, cross-sectional morphologies and the elemental distribution, respectively. The surface morphology of pitting was observed by Nikon MA200 Optical Microscope. Chemical compositions of the passive layer on the surface are analyzed by XPS (Thermo Fisher ESCALAB Xi+) with a monochromatic Al Kα X-ray source of 2 KeV at a take-off angle of 54.7°. The beam spot size was 500 μm. The pass energy was 20.0 eV with an energy step size of 0.1 eV. The measured binding energies were calibrated regarding the C 1s peak with a binding energy value of 284.8 eV.

2.3 Mechanical properties

Nanoindentation was carried out on a Ti950 TriboIndenter (Hysitron, Minneapolis, MN) using a calibrated diamond Berkovich indenter. Load control mode was set with the peak force of 5 mN with loading time of 5 s, holding time of 2 s, and unloading time of 5 s, respectively. 9 points were measured for each sample to obtain the average value of the results in order to ensure repeatability and reliability. The hardness H and reduced elastic modulus E_r were analyzed using the Oliver-Pharr method [31].

2.4 Electrochemical measurements

The electrochemical tests were performed in a 3.5 wt.% NaCl solution. A standard three-electrode electrochemical cell with a platinum foil as a counter electrode, Ag/AgCl as reference electrode, and the HEAs coated samples were used as working electrodes. All electrochemical tests were performed using the Metrohm Autolab workstation. Open-circuit potential (OCP) was recorded for 30 mins to reach a steady state. The electrochemical impedance spectroscopy (EIS) measurements were conducted at the OCP condition in a frequency range from 10^5 Hz down to 10^{-2} Hz with the amplitude of 10 mV, the impedance data were analyzed using Zsimpwin software. The potentiodynamic polarization measurements were carried out from -0.5 V_{OCP} to 1.0 V_{OCP} at a scan rate of 1 mV/s.

3. Results and discussion

3.1 Surface characterization

The top surface and cross-sectional morphologies of the multilayer TaNbHfZr/CoCrNi coating are shown in **Figure 1**. Nano-size round sheet-like granules for TaNbHfZr/CoCrNi coating were observed on the surface. For the composed CoCrNi monolayer, the columnar grains were confirmed from the cross-sectional SEM images as shown in **Figure 1 (b)**. It can be noted that the thickness of each monolayer was 100 nm, and the entire coating was 600 nm in thickness. The interfaces are explicitly presented (**Figure 1b**), to indicate the existence of the well-constructed multilayer structure. As shown in **Figure S1**, the strength of the TaNbHfZr/CoCrNi multilayer coating was ~27.5 N with no obvious peeling-off of the coating observed during the dynamic loading process, indicating a good adhesion strength between the coating and substrate. The columnar grains were separated by the amorphous TaNbHfZr layer, which can also be confirmed by the following TEM observation.

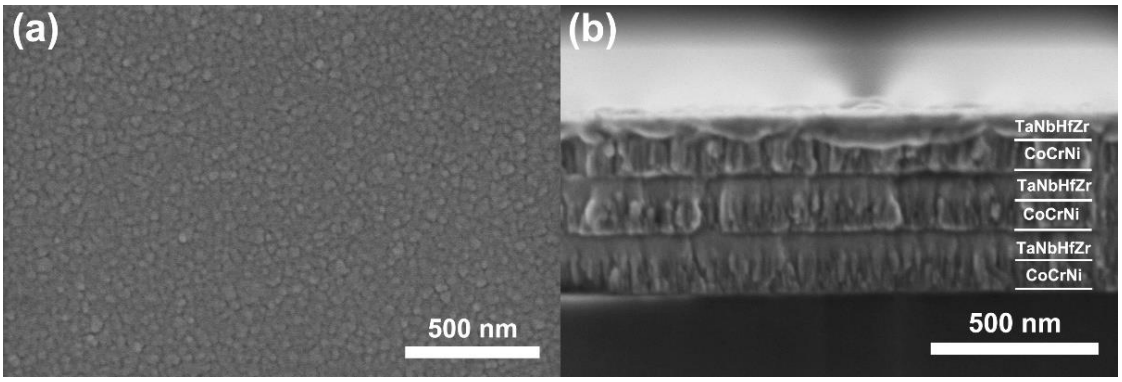

Figure 1 (a) Surface morphologies and **(b)** cross-sectional morphologies for TaNbHfZr/CoCrNi multilayer coating.

3.2 XRD measurements

The overall XRD patterns of CoCrNi, TaNbHfZr monolayer and TaNbHfZr/CoCrNi multilayer coatings are presented in **Figure 2**. After deducting the diffraction peaks for Si (111) substrate, the CoCrNi monolayer demonstrates a single fcc structure with (111) diffraction peak of preferred orientations at 44.1°. For TaNbHfZr monolayer, the broad steamed bun-like peak at 37.0° was detected, which confirms the amorphous feature. For TaNbHfZr/CoCrNi multilayer coating, two sets of diffraction peaks including the

crystalline CoCrNi and TaNbHfZr amorphous phase exist simultaneously. The diffraction peaks for fcc CoCrNi solid-solution is broad, suggesting that the grain size is small according to the Debye-Scherrer equation ($D = \frac{K\gamma}{B\cos\theta}$, where K is the Scherrer constant, D is the average grain size, γ is the wavelength of X-ray, θ is the Bragg angle), the results have good agreement with the SEM observation of the grain sizes as shown in **Figure 1 (a)**.

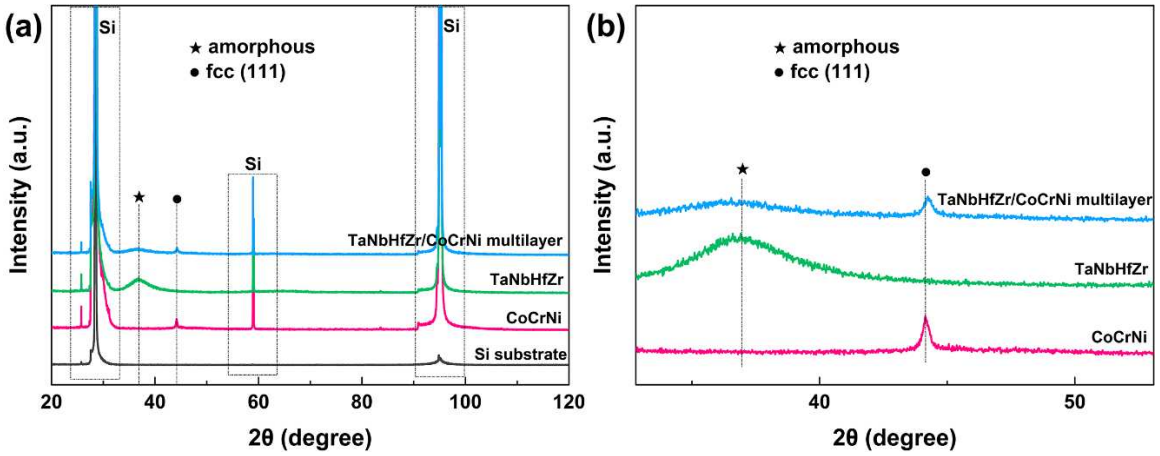

Figure 2 (a) XRD patterns; **(b)** enlarged XRD patterns of as-deposited CoCrNi and TaNbHfZr/CoCrNi coatings.

3.3 TEM analysis

The TEM characterization of the multilayer TaNbHfZr/CoCrNi coating is illustrated in **Figure 3**. Clear interfaces and well adhesion between each layer were observed in **Figures 3 (a)** and **(b),** suggesting the good compatibility between each deposited layer. SAED (Selected Area Electron Diffraction) image in **Figure 3 (c)** reveals that a combination of nano-polycrystalline (111), (200), (220), (311) of CoCrNi monolayer and no lattice phase contrast of amorphous TaNbHfZr monolayer were observed, which is consistent with the XRD patterns as shown in Figure 2. In the bright field (BF) image in **Figure 3 (b)** and DF (Dark Field) image shown in **Figure 3 (d)**, the grain size of 20 nm in width and grain boundaries were identified. The EDS mapping result in **Figure 3 (e)** implies that the multilayer coating has homogeneous elemental distribution without segregation and each TaNbHfZr or CoCrNi layer has the same chemical composition as shown in **Table 1**. The flat interfaces indicate good adhesion and

compatibility between each deposited layer.

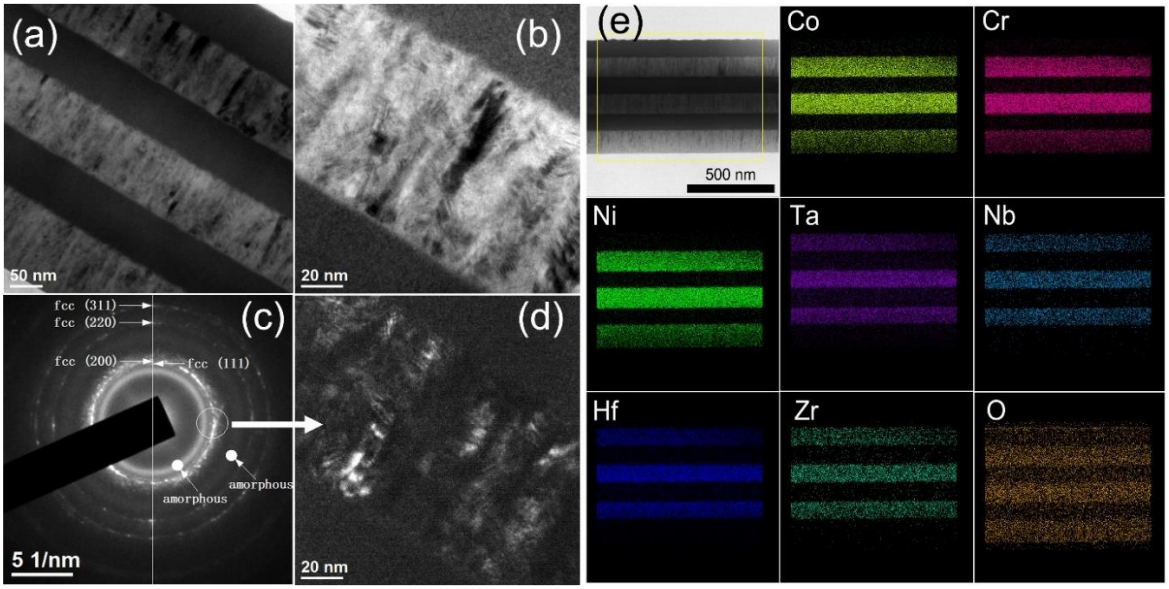

Figure 3 (a) Low and **(b)** high magnification morphologies of layer structure; **(c)** SAED (selected area electron diffraction) image; **(d)** DF (dark field) image corresponding to the selected diffraction spots circled in **(c)**, indicated by white arrow; **(e)** elemental distribution by EDS mapping for TaNbHfZr/CoCrNi multilayer coating.

Table 1 Elemental composition of TaNbHfZr and CoCrNi layer of the multilayer.

TaNbHfZr				**CoCrNi**		
Ta (at. %)	Nb (at. %)	Hf (at. %)	Zr (at. %)	Co (at. %)	Cr (at. %)	Ni (at. %)
27.27	29.62	22.81	20.30	29.59	36.42	33.98

3.4 Mechanical property

The nanoindentation tests at the peak load of 5 mN were carried out with the loading rate of 1 mN/s to compare the discrepancy of the mechanical behavior of CoCrNi and TaNbHfZr/CoCrNi coatings. The hardness and E_r are provided in **Figure 4**. The hardness is 7.67 GPa, 8.72 GPa and 8.24 GPa of TaNbHfZr, CoCrNi and TaNbHfZr/CoCrNi, respectively. In the amorphous TaNbHfZr, the shear bands cause the strain-softening due to the accumulation of the free volume by the inhomogeneous deformation [32]. For the multilayer coating, the introduction of the amorphous TaNbHfZr reduces the hardness, while the value is still higher than that in terms of the role-of-mixture indicating the interfaces play a role in the strengthening [33]. In the

nanoscale columnar grains, the dislocation needs to propagate within CoCrNi, thus the plastic yielding is determined by the required stress for single dislocation bowing via the confined layer slip (CLS) mechanism [32]. Besides, the interface may also have one or more arrays of misfit dislocations that will act as obstacles to CLS [34]. Microscopy results confirm that the CoCrNi monolayer is 100 nm in thickness, while the grain size is 20 nm which is less than the total layer thickness, suggesting that the strengthening came more from grain boundaries rather than phase interfaces. The interfaces cut off the continuously-grown coarse columnar grains refining the grain size of each CoCrNi layer according to the film growth theory thus the Hall-Petch strengthening dominates [35]. The deformation mechanism transits from grain boundary strengthening, dislocation strengthening and solid solution strengthening in nanocrystalline structure to shear transformation with lack of the internal interfaces and a poorer strain hardening capability in an amorphous structure [36, 37], therefore, the hardness was reduced slightly of the TaNbHfZr/CoCrNi multilayer than the CoCrNi monolayer coating. The phase interfaces with disordered structure bring the inelastic strain in dual-phase multilayer can be responsible for the reduced E_r [36, 38].

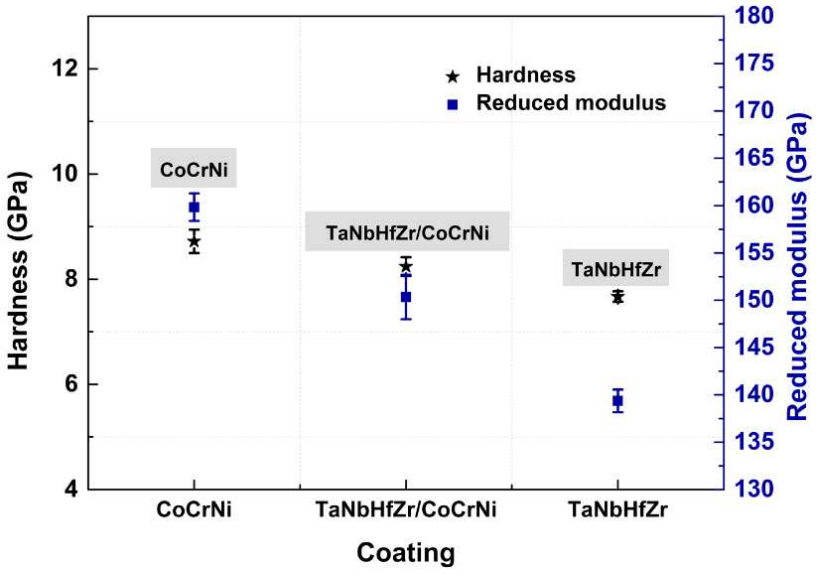

Figure 4 Nanoindentation hardness and E_r for CoCrNi, TaNbHfZr monolayer and TaNbHfZr/CoCrNi multilayer coatings.

3.5 Electrochemical performance

3.5.1 Potentiodynamic behavior of the samples immersed in a 3.5 wt. % NaCl solution

Figure 5 (a) displays OCP measurements of all the coatings for 1800 s and the typical potentiodynamic polarization curves of CoCrNi and TaNbHfZr/CoCrNi coatings immersed in the 3.5 wt.% NaCl solution at 25°C. It is clearly seen that the multilayer coating exhibits more noble OCP in the stable state suggesting less tendency to be corroded. Potentiodynamic polarization tests were employed to measure the susceptibility of the material to the pitting resistance [39]. A summary of corrosion potential (E_{corr}), current densities (i_{corr}) and pitting potential (E_{pit}) is provided in **Table 2**. The E_{corr} value of TaNbHfZr/CoCrNi multilayer coating is more positive compared to that of the monolayer CoCrNi coating. The i_{corr} value of TaNbHfZr/CoCrNi coating at the magnitude of 10^{-9} A/cm^2 is 2 orders lower than that of CoCrNi coating, suggesting that the TaNbHfZr/CoCrNi coating is less prone to be corroded under the current corrosive environment. A similar observation has been reported by Allahyarzadeh et al. [39] that the corrosive species can be delayed during the diffusion process due to the advantages of the multilayer structure. Therefore, compared with monolayer CoCrNi, the multilayered TaNbHfZr/CoCrNi coating remains a better protective capability to the substrate over a longer-time immersion in the solution.

Furthermore, the E_{pit} is denoted as the “knee” of the potential in the forward scan, where corresponds to a rapid increase in current with a small change in potential. When potential exceeds this value, pitting initiates, the more positive of E_{pit}, the more pitting resistant for the material. After 7 days immersion, the E_{pit} of 0.40 V was recorded for TaNbHfZr/CoCrNi coating, however, E_{pit} is not distinguished clearly for CoCrNi coating. Here, the E_{pit} value of CoCrNi coating is taken as the current density reaches 10 μA/cm^2 [40]. The E_{pit} of CoCrNi (0.68 V) is more noble than that of TaNbHfZr/CoCrNi (0.40 V), demonstrating a good resistance to pitting for CoCrNi monolayer coating. Further investigation should be carried out on the modification of the microstructure such as the modulation period or the modulation ratio to enhance the pitting resistance of the multilayer coating. For instance, the interfaces of the multilayer coating with a

smaller modulation period can more effectively block the penetration of corrosive species (water molecules, Cl^-).

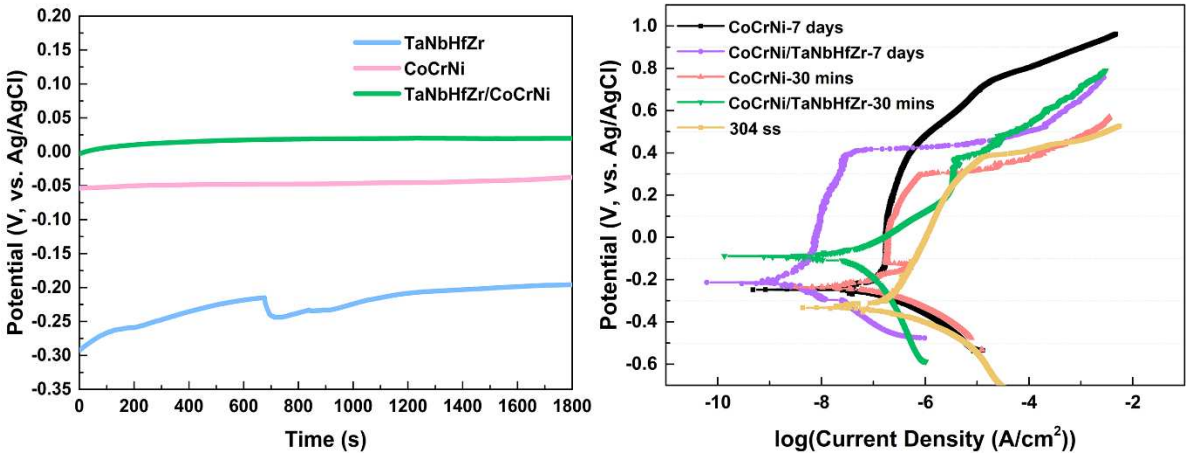

Figure 5 (a) OCP measurements for 30 mins, **(b)** typical potentiodynamic polarization plots for CoCrNi monolayer and TaNbHfZr/CoCrNi multilayer coatings after different immersion time in 3.5 wt.% NaCl solution.

Table 2 Electrochemical parameters obtained by potentiodynamic polarization tests for coatings immersed in the 3.5 wt.% NaCl solution at 25 °C after different immersion times.

Coating	Immersion time	E_{corr} (V, vs. Ag/AgCl)	i_{corr} (μA/cm²)	E_{pit} (V vs. Ag/AgCl)
CoCrNi	**30 mins**	-0.24±0.002	(5.79±0.942)×10^{-1}	0.30±0.010
	7 days	-0.25±0.002	(6.79±0.98)×10^{-1}	0.68±0.040
TaNbHfZr/CoCrNi	**30 mins**	-0.09±0.003	(7.8±0.65)×10^{-3}	0.34±0.014
	7 days	-0.21±0.006	(4.78±0.002)×10^{-3}	0.40±0.010

3.5.2 Electrochemical Impedance Spectroscopy (EIS)

EIS was carried out to explore the corrosion properties and electrochemical processes of CoCrNi monolayer and CoCrNi/TaNbHfZr multilayer coatings as shown in **Figure6**. As demonstrated in **Figure 6 (a)**, the shape of these coatings are capacitive semicircles and the TaNbHfZr/CoCrNi coating has the largest semicircle after 7 days of exposure compared to that of 30 mins, indicating the increase in the corrosion resistance after long immersion. The Bode phase diagram implicates two time constants representing the rate of the electrochemical reactions [39] thus we utilized two RC components in the equivalent electrical circuit (EEC). The EEC model adopted

for fitting the EIS data is $R_s(Q_1(R_1(Q_2R_2)))$ as shown in **Figure 6 (a)** and the fitting quality is good with small chi-square values. The detailed fitted parameters are displayed in **Table 3**.

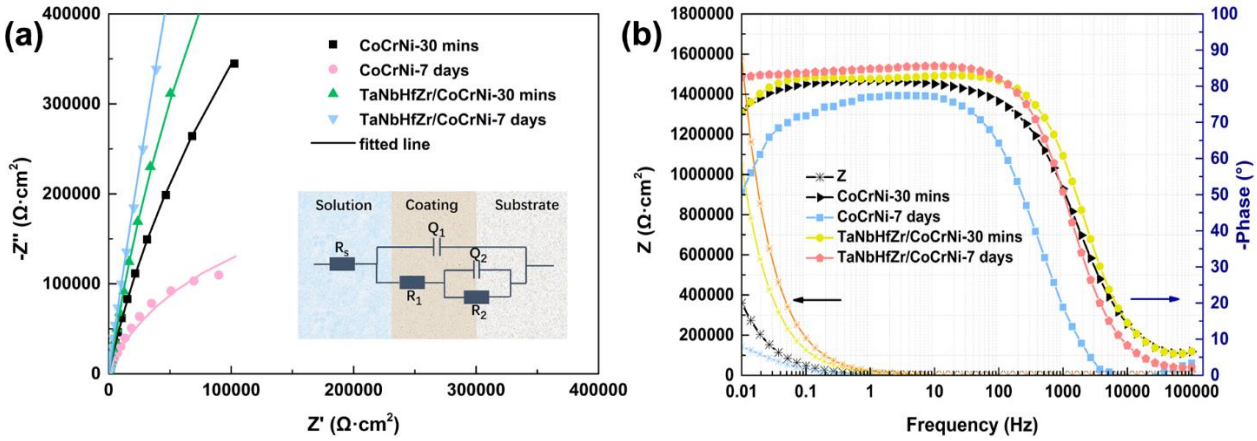

Figure 6 (a) Experimental and fitted Nyquist plots; **(b)** Bode plots for CoCrNi monolayer and TaNbHfZr/CoCrNi multilayer coatings.

R_s represents the solution resistance. The constant phase element *CPE* in the equivalent circuit, designated as Q_1 and Q_2, describing the frequency dispersion and deviation from the ideal dielectric behavior caused by the surface heterogeneity of the electrode, is expressed as [41, 42]

$$Z_{CPE} = \frac{1}{Y_0(j\omega)^n} \qquad \textbf{Equation 1}$$

Where, Y_0 (Q) is the magnitude of *CPE*, ω is the angular frequency and n is the deviation parameter which lies in a value region between 0 and 1. when n = 1, the *CPE* is considered as an ideal capacitor; when 0.5 < n < 1, the *CPE* describes a distribution of dielectric relaxation times in frequency space; When n = 0.5, the *CPE* represents a Warburg impedance. Here, the parameter of *CPE* represents the surface heterogeneity indicating the compactness of the coating and a lower Y_0 reveals the formation of a more homogeneous and less defective oxide film on the surface. The smaller R_2 and bigger Y_0 (Q_2) suggest the corrosion processes at the inner interfaces were more heterogeneous [43].

Table 3 Fitted results of the EIS data.

Coating	R_s	Q_1	R_1	Q_2	R_2 (Ω·cm²)	Chsq

(immersion time)	($\Omega \cdot cm^2$)	Y_0 ($\mu F \cdot s^{n-1} \cdot cm^{-2}$)	n	($\Omega \cdot cm^2$)	Y_0 ($\mu F \cdot s^{n-1} \cdot cm^{-2}$)	n		
CoCrNi (30 mins)	6.55±0.03	19.54±0.56	0.91± 0.002	8.38±0.02	12.60± 0.09	0.90± 0.01	(2.76± 0.06)×10^6	4.3×10^{-4}
CoCrNi (7 days)	26.64±1.49	18.44±0.12	0.98± 0.020	(3.37± 0.05)×10^2	29.30± 0.08	0.73± 0.02	(4.73± 0.04)×10^5	3.5×10^{-3}
TaNbHfZr/CoCrNi (30 mins)	11.53±0.16	11.05±0.03	0.94± 0.003	(1.03± 0.02)×10^5	1.24± 0.02	0.90± 0.02	(5.32± 0.05)×10^6	5.3×10^{-4}
TaNbHfZr/CoCrNi (7 days)	21.39±0.35	7.57±0.06	0.96± 0.003	(1.59± 0.03)×10^5	0.88± 0.02	0.72± 0.01	(4.99± 0.02)×10^8	3.7×10^{-5}

The whole polarization resistance for the system R_p, an index representing the corrosion resistance of the coating system, was calculated via the following formula [44]

$$R_p = R_1 + R_2 \qquad \textbf{Equation 2}$$

R_1 and Q_1 represent the electric double layer resistance and capacitance between the HEA coatings and the solution at the high frequency, R_2 and Q_2 are the charge transfer resistance and the double-layer capacitance of the inner interfaces between the film and the substrate at the low frequency. The lower R_p of TaNbHfZr/CoCrNi coating signifies that the reduced corrosion resistance, the opposite trend of CoCrNi coating interpreting the fact that TaNbHfZr/CoCrNi coating benefits from the multilayer structure.

In the Bode plots as shown in **Figure 6 (b)**, the impedance modulus remains a straight line and the phase angle is close to zero at high-frequency ranges, indicating the resistive-like behavior. At the relatively low frequencies, a slanted impedance modulus and a maximum phase angle are reached, indicating the capacitive-like behavior [45]. The higher the maximum phase angle, the better the corrosion properties. The multilayer coating of TaNbHfZr/CoCrNi after 7 days' immersion possesses the superior corrosion resistance with |Z| of 1.5×10^6 $\Omega \cdot cm^2$ and the largest maximum phase angle (85 °) at low and medium frequencies from 0.01 Hz to ~100 Hz. The |Z| values at the frequency of 0.1 Hz corresponds to the polarization resistance which reflects the corrosion resistance of the alloy in the solution [2]. The |Z| value of TaNbHfZr/CoCrNi at 0.1 Hz is higher than that of CoCrNi coating after different immersion times as

exhibited in **Figure 6 (b)**, suggesting that the corrosion resistance of TaNbHfZr/CoCrNi multilayer coating is better.

3.6 Characterization of the passive films

3.6.1 XPS result of the passive films

To further examine the oxidation state of the passive film formed on the surface after 7 days' immersion, XPS analysis was conducted. The high-resolution spectrum of Ta 4f, Nb 3d, Hf 4f, Zr 3d and O 1s at the top surface are presented in **Figure 7**. To improve the accuracy of the result, all the data has been calibrated by the stand binding energy of C 1s peak of 284.8 eV. The Ta 4f spectrum split into the peaks at 27.62 eV and 25.73 eV corresponds to Ta $4f_{5/2}$ and Ta $4f_{7/2}$ of Ta_2O_5, simultaneously minor Ta_2O_3 (23.60 eV) exists. The Nb $3d_{3/2}$ (209.57 eV) and Nb $3d_{5/2}$ (206.85 eV) of the full oxide Nb_2O_5 accompanied by minor suboxide NbO_2 (205.63 eV) and NbO (204.10 eV), the Hf $4f_{5/2}$ (18.16 eV) and Hf $4f_{7/2}$ (16.50 eV) for the full oxide HfO_2, the Zr $3d_{3/2}$ (184.33 eV) and Zr $3d_{5/2}$ (181.95 eV) for full oxide ZrO_2 were also detected on the surface. The results confirmed the stable chemical state of the oxide formed on the surface, which is a vital contribution to the passive performance of TaNbHfZr/CoCrNi coating. Apart from the oxides, the metallic states of Ta, Nb, Hf and Zr were also detected. The percentage of the compositional oxides within the passive films for TaNbHfZr/CoCrNi coating exhibits that the accounts of ZrO_x (32.72 at. %) are higher than those of TaO_x (19.76 at. %), NbO_x (22.34 at. %) and HfO_x (25.18 at. %). Moreover, the O 1s spectra are split into three peaks including O^{2-} (529.92 eV) species, OH^- (531.19 eV) species and a small percentage of H_2O (531.98 eV) species, suggesting the main presence of oxide and hydroxide on the surface of the coatings with minor bound water to capture the dissolving metal ions forming a new film resisting further corrosive attack [46]. For 7-day immersed CoCrNi monolayer coating, as can be seen in **Figure S2**, the Cr forms the major oxide in the passive films and CrO_x accounts for ~52 at. %, indicating Cr played a critical role in the anti-corrosion performance. The composition differences of the passive films between CoCrNi monolayer and TaNbHfZr/CoCrNi multilayer coatings are one of the factors that affect

their corrosion resistance.

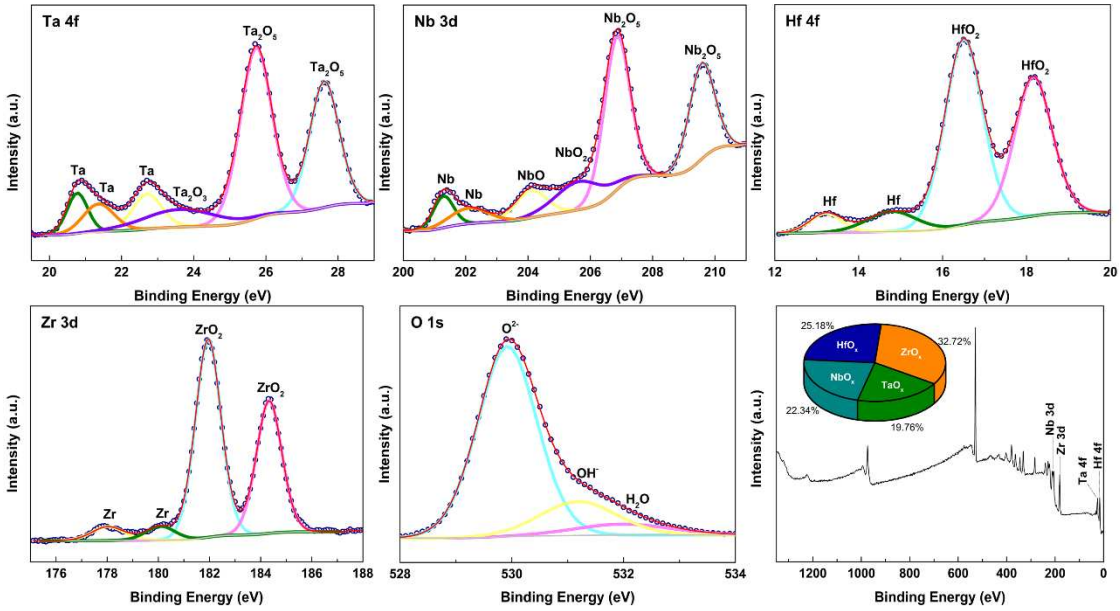

Figure 7 XPS spectrum obtained after etching for 120 s by Ar^+ of Ta 4f, Nb 3d, Hf 4f, Zr 3d and O1s for TaNbHfZr/CoCrNi multilayer coating after immersion of 7 days in the 3.5 wt.% NaCl solution.

3.6.2 TEM-EDS line scan for the passive film

The formation of the passive films relates to the enhancement in corrosion properties of HEAs. The morphology and elemental composition of the passive film were scanned via TEM and EDX, the results are provided in **Figure 8.** The presence of a high concentration of oxygen was confirmed that the oxidation layer with several nanometers in thickness was detected on the surface. The elements of Ta, Nb, Hf and Zr are apt to form the oxidation layer, due to the low Gibbs energy $\Delta_f G^0$ with oxygen (Ta_2O_5: -1911.2 KJ/mol Nb_2O_5: -1766.0 KJ/mol, HfO_2: -1088.2 KJ/mol, ZrO_2: -1042.8 KJ/mol) [47]. Additionally, it can be noted that the formation of the oxidation layers is inhomogeneous, confirming that the passive film has weak sites to break down when samples immersed in the Cl^- containing environment [48].

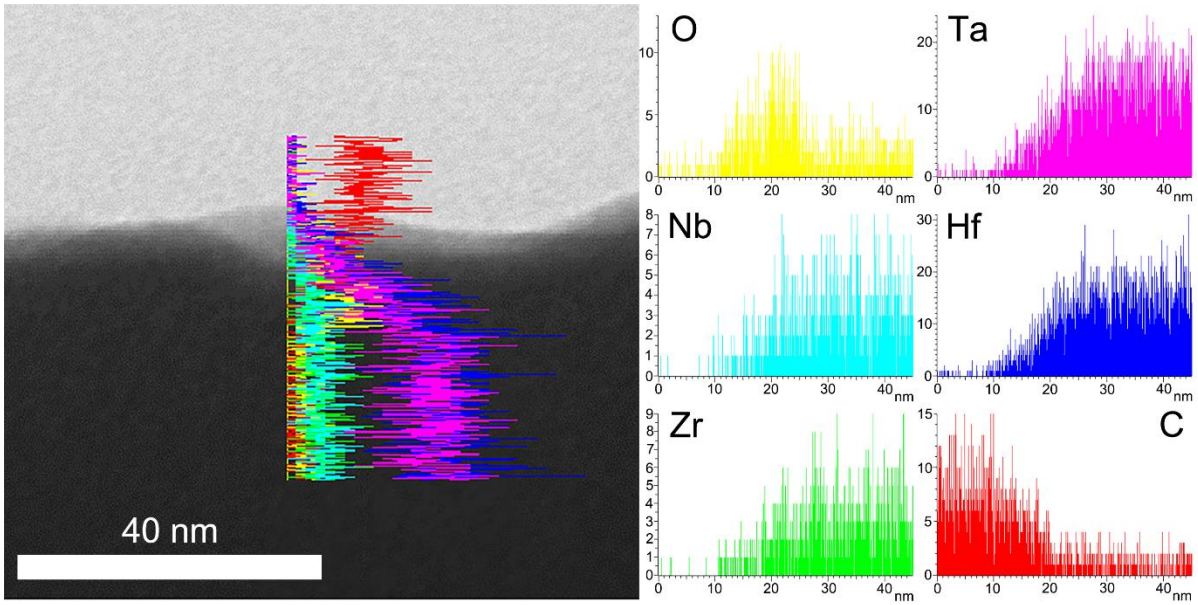

Figure 8 The TEM image and TEM-EDS line scan result for the top surface of as-deposited TaNbHfZr/CoCrNi multilayer film.

The effective passive film thickness h_{eff} can be calculated using the following relation [49-51]:

$$h_{eff} = \frac{\varepsilon \varepsilon_0 A}{C_{eff}} \qquad \textbf{Equation 3}$$

where A is the surface area of the passive film and the effective area is twice of the geometric area assuming the roughness factor is 2 for the polished specimen [49], ε is the dielectric constant and the chosen value is 30 for thin films [51, 52], ε_0 is the vacuum permittivity (8.8542×10^{-14} F/cm), C_{eff} is the effective capacitance of the passive film extracted from the *CPE* element to interpret the film properties. The C_{eff} can be obtained by the following equation [49]:

$$C_{eff} = Y_0^{\frac{1}{n}} R_s^{\frac{1-n}{n}} \qquad \textbf{Equation 4}$$

where Y_0 is the magnitude of *CPE*, R_s is the solution resistance, and n is the dispersion coefficient. The calculated values of C_{eff} and h_{eff} according to **Equations 3** and **4** are shown in **Table 4**, exhibiting that the thickness of the passive film on the CoCrNi and TaNbHfZr/CoCrNi coatings are 1.88 nm and 4.42 nm after 30 mins' immersion, and 2.88 nm and 5.75 nm after 7 days' immersion, respectively. The thickness of the passive film on the multilayer coating of TaNbHfZr/CoCrNi is thicker than that of CoCrNi monolayer coating, which contributes to the improved corrosion performance

of the multilayer structure.

Table 4 *CPE*1 parameters, resistance, effective capacitance and thickness of passive films formed on the monolayer and multilayer coatings after different immersion times.

Immersion time	Coating	C_{eff} (μF/cm^2)	h_{eff} (nm)
30 mins	CoCrNi	31.83±1.19	1.88±0.07
	TaNbHfZr/CoCrNi	15.26±0.19	4.42±0.06
7 days	CoCrNi	18.48±0.05	2.88±0.02
	TaNbHfZr/CoCrNi	9.24±0.16	5.75±0.10

The excellent corrosion protection of the multiplayer coatings comes from the novel multilayer structure. It is well-known that grain boundaries provide more paths for vacancies transport with an irregular atom array. Compared with the crystalline monolayer, the notable enhancement of the corrosion resistance of multilayer coatings with lower i_{corr} and more noble E_{corr} can be ascribed by the existence of the multilayer structure, in which the introduction of the amorphous TaNbHfZr layer without any ready path cut off the diffusion tunnel for localized attack by Cl^-. The interfaces not only cut off the continuous grain boundaries along the texture direction as the hindrance for transporting Cl^-, but also prohibit and block the active sites, resulting in good general corrosion resistance.

3.7 Characterization of pitting behavior

Figure 9 exhibits the surface morphologies of CoCrNi monolayer and TaNbHfZr/CoCrNi multilayer coatings after the polarization measurements. To further obtain the depth and compositional distribution of the pits on the surface, 3D profilometry measurement and EDS mapping were carried out, and the results are demonstrated in **Figure 10**. The maximum pitting depth is denoted as h_{max}, and the values of h_{max} for CoCrNi and TaNbHfZr/CoCrNi were 117 μm and 131 μm, respectively. The average pit depth of $\bar{h}$ for CoCrNi coating was 105.2 ± 6.37 μm, and 119.3 ± 10.22 μm for TaNbHfZr/CoCrNi coating. The EDS mapping results show that the apparent contrast difference for intrinsic compositional elements of the coatings and 304 SS (*e.g.* Fe), where the substrate was observed, confirming that the coatings were destroyed after the polarization.

As exhibited in **Figures 9 and 10**, fewer and deeper pits appeared on the surface of TaNbHfZr/CoCrNi multilayer coating, while the shallower pits were observed on the CoCrNi monolayer coating surface. The results suggest that the multilayer structure prevents the initiation and propagation of pitting by blocking the corrosive species. *i.e.* grain boundaries or micro-pores which can be disconnected and provided less diffusion channels to transport the corrosive medium, thus pits with less density were observed on the TaNbHfZ/CoCrNi multilayer coating.

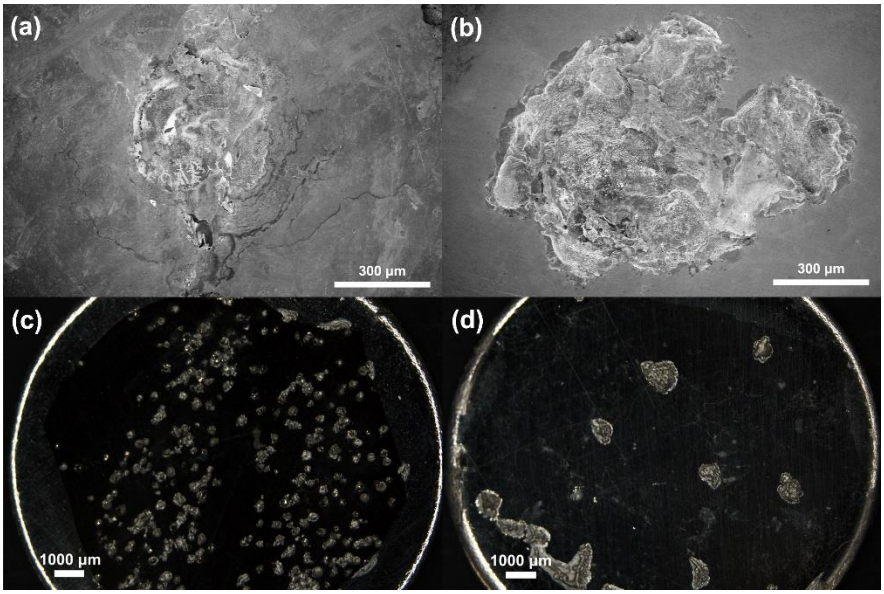

Figure 9 SEM images for the typical pitting morphologies on the surface of **(a)** CoCrNi and **(b)** TaNbHfZr/CoCrNi multilayer coatings after potentiodynamic polarization test; whole surface morphologies of pitting of **(c)** CoCrNi monolayer and **(d)** TaNbHfZr/CoCrNi multilayer coatings after potentiodynamic polarization.

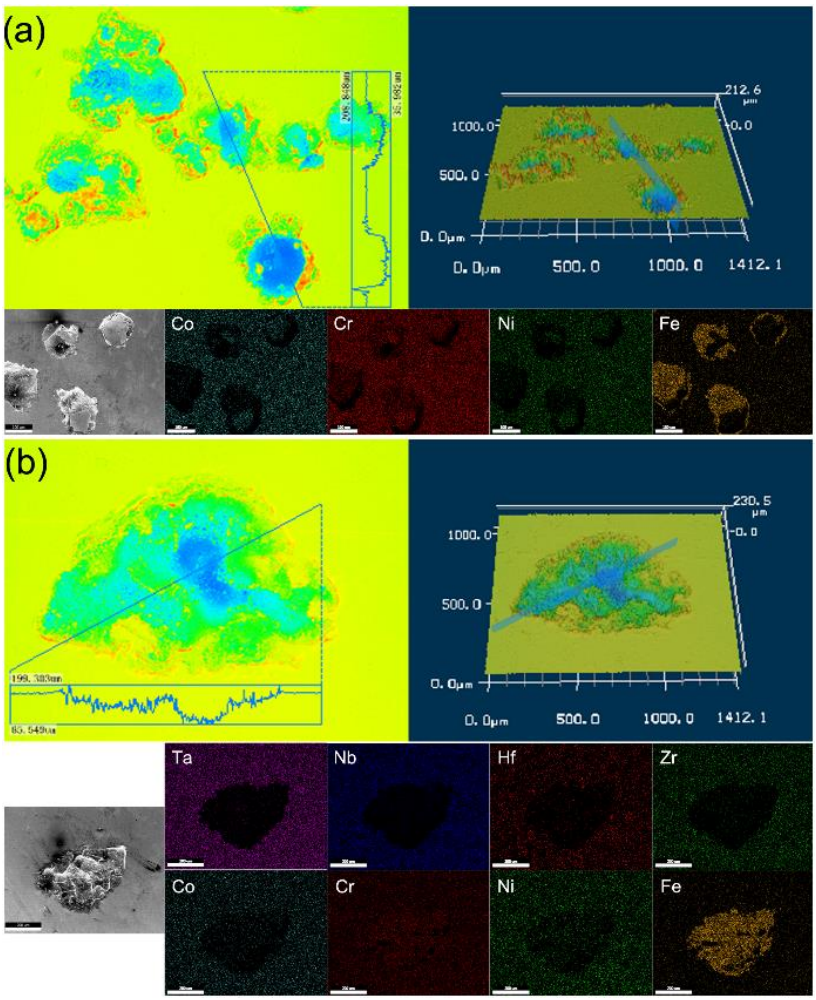

Figure 10 Typical 3D morphology and elemental distributions for pitting of **(a)** CoCrNi and **(b)** TaNbHfZr/CoCrNi multilayer coatings.

Galvanic corrosion plays a vital matter to understand the development of localized corrosion, according to the conception of galvanic corrosion that occurs when the electrically coupled dissimilar metals exposed in a corrosive environment [53, 54], CoCrNi monolayer coating has been less affected by the galvanic corrosion based on the same constituent Cr element with the substrate. The continuous columnar grains provide plenty of grain boundaries, which are considered as the diffusion channels and potentially prone sites for pitting [55, 56], increasing the localized corrosion. By contrast, the introduction of TaNbHfZr into the multilayer deteriorates the resistance to the localized corrosion via the mutual function of galvanic corrosion between each interlayer. TaNbHfZr coating with less noble E_{corr} (-0.40 V) acts as the anode upon coupling compared to that of CoCrNi sublayer (-0.24 V) and steel substrate (-0.33 V)

and will be preferentially dissolved. As shown in the schematic diagram in **Figure 11**, the multilayer interfaces act as the diffusion barriers and block the corrosion medium to the surface, and the interconnected pores or cracks can be reduced via the existence of interfaces in the multilayer [57]. Furthermore, the interfaces allow spreading of the corrosive medium laterally, delaying the attack to the substrate and lagging the corrosion rate in the multilayer coating [58]. However, once the corrosive medium reaches the substrate, galvanic corrosion will be triggered among TaNbHfZr layer, CoCrNi layer and the substrate, in which case the TaNbHfZr layer corrodes preferentially and accelerates both the penetration of corrosive medium and pit propagation of the surface. Another point worth mentioning during the pitting process is the stress caused by the increased volume due to the corrosion products [59]. The existed products within the corroded layers provide high stresses between the interfaces or each layer [59], accelerating the enlargement of the pitting size or microcracks.

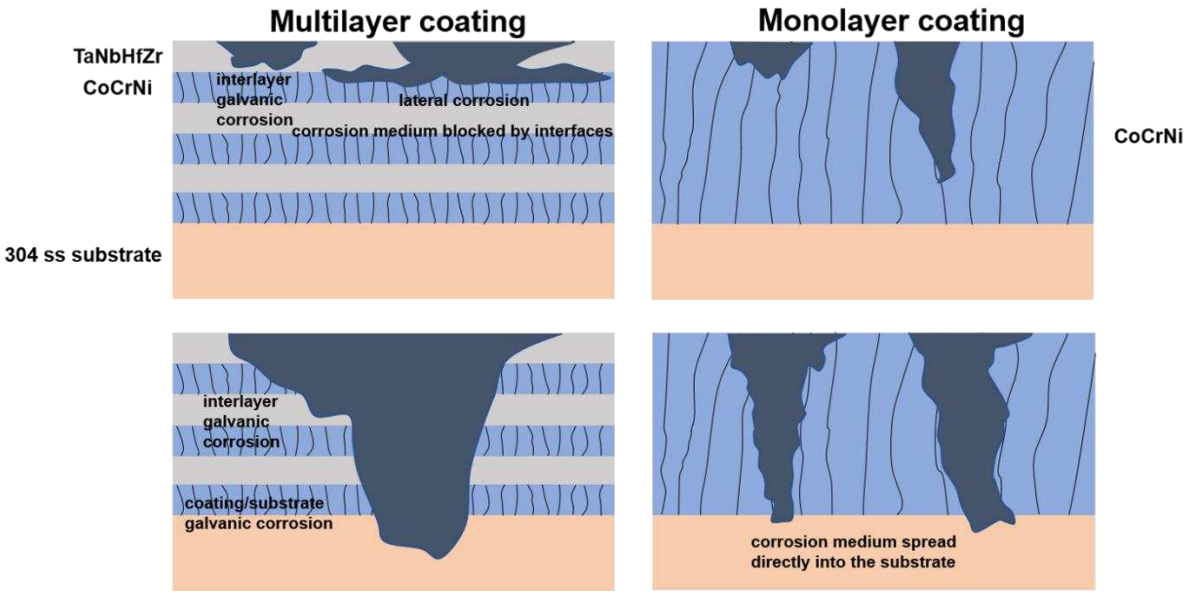

Figure 11 Schematic diagram of corrosion mechanisms in TaNbHfZr/CoCrNi multilayer and CoCrNi monolayer coatings.

Furthermore, the presence of a high concentration of Cr within CoCrNi coating provides the dissolution of Cr^{3+} ions, which can effectively accelerate the formation of the passive film as confirmed in **Figure S2** with preferable resistance against the

pitting corrosion based on the self-repairing, stable and adherent capability of the passive film [60, 61]. For the multilayer coating of TaNbHfZr/CoCrNi, the top layer of TaNbHfZr has a slow growth rate and inferior recovery ability of the passive film compared to that of CoCrNi coating. Therefore, further work should be considered on the modification of the composition or sequences of each layer to enhance the pitting resistance of the multilayer coating.

3.7.1 Cl^- penetration

The passive films are generated by the oxidation of the compositional elements on the surface and act as a protection layer against corrosion. After the breakdown of the passivity, the pitting corrosion can be attributed to the fact that the anodic sites with fast metal dissolution, but the corresponding cathodic sites can be spread out over a wide range [62]. The related processes can be expressed using the equations as follows:

$$Me \rightarrow Me^{n+} + ne^- \quad \textbf{Equation 6}$$

$$O_2 + 2H_2O + 4e^- \rightarrow 4OH^- \quad \textbf{Equation 7}$$

where “Me” represents compositional metals in the coatings, **Equation 6** denotes the anode reaction in which the metals dissolve and the **Equation 7** signifies the cathode reaction with the electron conduction. The passive films are in dynamic equilibrium between film growth and dissolution, among which the dissolution of the film is the electrochemical reaction accompanied by the generation of metal cations [63]. The positively charged metallic ions Ta^{5+}, Nb^{5+}, Hf^{4+} and Zr^{4+} flow into the solution, simultaneously the negatively charged free electron e^- pass through the pore solution to the cathode (passive areas), where they are absorbed by oxygen and water to form hydroxyl ions (cathodic reaction).

Chlorides enter the pore either by diffusion (in stationary pore water) or by capillary suction of the surface water [64, 65]. The corresponding reactions of Cl^- are:

$$Me^{n+} + nCl^- \rightarrow MeCl_n \quad \textbf{Equation 8}$$

$$MeCl_n + nH_2O \rightarrow Me(OH)_n + nH^+ + nCl^- \quad \textbf{Equation 9}$$

It is well known that the Cl^- ions possess high permeability with a small ionic radius

and can be easily absorbed on the surface of metals as confirmed by **Equation 8**. Local acidification occurs through the hydrolysis of the metal cations, and Cl^- migrate into the pit to balance the charge of the dissolved metal cations and maintain electroneutrality as evidenced by **Equation 9** [66]. The absorption and accumulation of Cl^- increase the donor density of the formed passive film causing a larger potential drop at the film/solution interface, which accelerates the dissolution of the passive film and enlarges or deepens the pitting sites [44]. Additionally, the penetration of Cl^- remarkably modifies the interface via lattice expansion and induces undulation at the material interface [48]. For the multilayer coating of TaNbHfZr/CoCrNi, the introduction of an amorphous TaNbHfZr layer acts as a barrier to reduce the diffusion of Cl^- ions. On the other hand, the multilayer structure decreases the corrosion behaviour by increasing the hindrance between the corrosion environment and the substrate. However, once the pitting occurs, the less anti-corrosive against pitting is the major deficiency for the multilayer coating. Therefore, further work needs to be done to enhance the pitting resistance regarding the optimization of the structure or the chemical composition of the multilayer coating.

4. Conclusion

In this work, we firstly designed and prepared the TaNbHfZr/CoCrNi multilayer coating with amorphous/fcc bi-phase structure combining the concept of high entropy metallic glass with the medium entropy alloy in an anti-corrosive coating system by magnetron sputtering. The passivation behaviour and mechanical properties of the coating have been systematically studied via a series of electrochemical methods and advanced surface analysis. The nanoindentation results indicate that the hardness reduced due to the softening of the shear band induced by the amorphous TaNbHfZr layer and the decreased E_r is the result of the brought inelastic strain by the interfaces. The interface blocking and Hall-Petch strengthening play a joint role in the multilayer strengthening. In a 3.5 wt.% NaCl environment, the corrosion performance of the TaNbHfZr/CoCrNi multilayer coating indicates a more noble corrosion potential and lower current density compared with CoCrNi monolayer coating. The novel multilayer structure plays a key

role in corrosion enhancement where the multi-principal components ensure excellent mechanical property and an effective protection mechanism of the Cl^- ions induced localized corrosion even in a long-term immersion. However, further work should be focused on the modification of the microstructure, to enhance the pitting resistance of the multilayer coating.

Declaration of competing interest

On behalf of all the authors, we declare that we have no declarations of interest.

Acknowledgments

This work was supported by the Natural Science Foundation of Shaanxi Province (No. 2019TD-020).

References

[1] J.W. Yeh, S.K. Chen, S.J. Lin, J.Y. Gan, T.S. Chin, T.T. Shun, C.H. Tsau, S.Y. Chang, Nanostructured high-entropy alloys with multiple principal elements: novel alloy design concepts and outcomes, Adv. Eng. Mater., 6 (2004) 299-303.

[2] H. Luo, Z. Li, A.M. Mingers, D. Raabe, Corrosion behavior of an equiatomic CoCrFeMnNi high-entropy alloy compared with 304 stainless steel in sulfuric acid solution, Corros. Sci., 134 (2018) 131-139.

[3] P. Muangtong, A. Rodchanarowan, D. Chaysuwan, N. Chanlek, R. Goodall, The corrosion behaviour of CoCrFeNi-x (x = Cu, Al, Sn) high entropy alloy systems in chloride solution, Corros. Sci., 172 (2020).

[4] O.N. Senkov, G.B. Wilks, D.B. Miracle, C.P. Chuang, P.K. Liaw, Refractory high-entropy alloys, Intermetallics, 18 (2010) 1758-1765.

[5] A. Karati, K. Guruvidyathri, V.S. Hariharan, B.S. Murty, Thermal stability of AlCoFeMnNi high-entropy alloy, Scr. Mater., 162 (2019) 465-467.

[6] D.B. Miracle, O.N. Senkov, A critical review of high entropy alloys and related concepts, Acta Mater., 122 (2017) 448-511.

[7] M.H. Tsai, J.W. Yeh, High-entropy alloys: A critical review, Mater. Res. Lett., 2 (2014) 107-123.

[8] Y. Qiu, S. Thomas, M.A. Gibson, H.L. Fraser, N. Birbilis, Corrosion of high entropy alloys, npj Mater. Degrad., 1 (2017) 15.

[9] B.R. Song, Y.H. Li, K.H. Wang, Z.H. Cong, B. Gao, Z.X. Song, J. Chen, Nano-mechanical properties of TaNbHfZr metallic glass films, Surf. Eng., 35 (2019) 728-735.

[10] Y. Shi, B. Yang, P.K. Liaw, Corrosion-resistant high-entropy alloys: a review, Metals-Basel, 7 (2017).

[11] J. Wang, W. Li, H. Yang, H. Huang, S. Ji, J. Ruan, Z. Liu, Corrosion behavior of CoCrNi medium-entropy alloy compared with 304 stainless steel in H2SO4 and NaOH solutions, Corros. Sci., 177 (2020).

[12] K. Feng, Y. Zhang, Z. Li, C. Yao, L. Yao, C. Fan, Corrosion properties of laser cladded CrCoNi medium entropy alloy coating, Surf. Coat. Tech., 397 (2020).

[13] S. Zhang, C.L. Wu, C.H. Zhang, M. Guan, J.Z. Tan, Laser surface alloying of FeCoCrAlNi high-entropy alloy on 304 stainless steel to enhance corrosion and cavitation erosion resistance, Opt. Laser Technol., 84 (2016) 23-31.

[14] F. Cao, P. Munroe, Z. Zhou, Z. Xie, Medium entropy alloy CoCrNi coatings: Enhancing hardness and damage-tolerance through a nanotwinned structuring, Surf. Coat. Tech., 335 (2018) 257-264.

[15] Z. Wu, H. Bei, F. Otto, G.M. Pharr, E.P. George, Recovery, recrystallization, grain growth and phase stability of a family of FCC-structured multi-component equiatomic solid solution alloys, Intermetallics, 46 (2014) 131-140.
[16] M.A. Ezazi, M.M. Quazi, E. Zalnezhad, A.A.D. Sarhan, Enhancing the tribo-mechanical properties of aerospace AL7075-T6 by magnetron-sputtered Ti/TiN, Cr/CrN & TiCr/TiCrN thin film ceramic coatings, Ceram. Int., 40 (2014) 15603-15615.
[17] R.D. Arnell, P.J. Kelly, Recent advances in magnetron sputtering, Surf. Coat. Tech., 112 (1999) 170-176.
[18] A.A. Voevodin, J.P. O'Neill, J.S. Zabinski, Nanocomposite tribological coatings for aerospace applications, Surf. Coat. Tech., 116-119 (1999) 36-45.
[19] P.E. Hovsepian, Q. Luo, G. Robinson, M. Pittman, M. Howarth, D. Doerwald, R. Tietema, W.M. Sim, A. Deeming, T. Zeus, TiAlN/VN superlattice structured PVD coatings: a new alternative in machining of aluminium alloys for aerospace and automotive components, Surf. Coat. Tech., 201 (2006) 265-272.
[20] V.V.A. Thampi, A. Bendavid, B. Subramanian, Nanostructured TiCrN thin films by pulsed magnetron sputtering for cutting tool applications, Ceram. Int., 42 (2016) 9940-9948.
[21] S. Hong, S.H. Kang, Y. Kim, C.W. Jung, Transparent and flexible antenna for wearable glasses applications, IEEE T. Antenn Propag., 64 (2016) 2797-2804.
[22] W. Li, P. Liu, P.K. Liaw, Microstructures and properties of high-entropy alloy films and coatings: a review, Mater. Res. Lett., 6 (2018) 199-229.
[23] Z. An, H. Jia, Y. Wu, P.D. Rack, A.D. Patchen, Y. Liu, Y. Ren, N. Li, P.K. Liaw, Solid-solution CrCoCuFeNi high-entropy alloy thin films synthesized by sputter deposition, Mater. Res. Lett., 3 (2015) 203-209.
[24] L. Liu, J.B. Zhu, C. Hou, J.C. Li, Q. Jiang, Dense and smooth amorphous films of multicomponent FeCoNiCuVZrAl high-entropy alloy deposited by direct current magnetron sputtering, Mater. Design, 46 (2013) 675-679.
[25] Y. Yan, J. Lee, X.L. Cui, Enhanced photoelectrochemical properties of Ta-TiO2 nanotube arrays prepared by magnetron sputtering, Vacuum, 138 (2017) 30-38.
[26] J.H. Huang, C.H. Ma, H. Chen, Effect of Ti interlayer on the residual stress and texture development of TiN thin films deposited by unbalanced magnetron sputtering, Surf. Coat. Technol., 201 (2006) 3199-3204.
[27] J. Creus, H. Idrissi, H. Mazille, F. Sanchette, P. Jacquot, Improvement of the corrosion resistance of CrN coated steel by an interlayer, Surf. Coat. Tech., 107 (1998) 183-190.
[28] S. Guo, C.T. Liu, Phase stability in high entropy alloys: formation of solid-solution phase or amorphous phase, Prog. Nat. Sci-Mater., 21 (2011) 433-446.
[29] Z. Li, C.H. Liu, Q.S. Chen, J.J. Yang, J.M. Liu, H.Y. Yang, W. Zhang, R.Q. Zhang, L.X. He, J.P. Long, H. Chang, Microstructure, high-temperature corrosion and steam oxidation properties of Cr/CrN multilayer coatings prepared by magnetron sputtering, Corros. Sci., 191 (2021).
[30] R.Z. Li, S.H. Wang, J.B. Pu, D.P. Zhou, M. Yu, Y. Wei, W.M. Guo, Study of NaCl-induced hot-corrosion behavior of TiN single-layer and TiN/Ti multilayer coatings at 500 °C, Corros. Sci., 192 (2021).
[31] W.C. Oliver, G.M. Pharr, An improved technique for determining hardness and elastic-modulus using load and displacement sensing indentation experiments, J. Mater. Res., 7 (1992) 1564-1583.
[32] N.G. Chechenin, J. Bottiger, J.P. Krog, Nanoindentation of amorphous aluminum oxide films I. The influence of the substrate on the plastic properties, Thin Solid Films, 261 (1995) 219-227.
[33] M. Callisti, T. Polcar, Combined size and texture-dependent deformation and strengthening mechanisms in Zr/Nb nano-multilayers, Acta Mater., 124 (2017) 247-260.
[34] W.D. Nix, Yielding and strain hardening of thin metal films on substrates, Scr. Mater., 39 545.
[35] W.H. Liu, Y. Wu, J.Y. He, T.G. Nieh, Z.P. Lu, Grain growth and the Hall–Petch relationship in a high-

entropy FeCrNiCoMn alloy, Scripta Mater., 68 (2013) 526-529.
[36] Z.H. Cao, Y.J. Ma, Y.P. Cai, G.J. Wang, X.K. Meng, High strength dual-phase high entropy alloys with a tunable nanolayer thickness, Scr. Mater., 173 (2019) 149-153.
[37] Z. Fu, W. Chen, H. Wen, D. Zhang, Z. Chen, B. Zheng, Y. Zhou, E.J. Lavernia, Microstructure and strengthening mechanisms in an FCC structured single-phase nanocrystalline Co25Ni25Fe25Al7.5Cu17.5 high-entropy alloy, Acta Mater., 107 (2016) 59-71.
[38] P. Goudeau, P. Villain, T. Girardeau, P.O. Renault, K.F. Badawi, Elastic constants investigation by X-ray diffraction of in situ deformed metallic multi-layers, Scr. Mater., 50 (2004) 723-727.
[39] M.H. Allahyarzadeh, M. Aliofkhazraei, A.S. Rouhaghdam, V. Torabinejad, H. Alimadadi, A. Ashrafi, Electrodeposition mechanism and corrosion behavior of multilayer nanocrystalline nickel-tungsten alloy, Electrochim. Acta, 258 (2017) 883-899.
[40] S. Eriksson, H.P. Hermansson, Pitting corrosion of copper in nuclear waste disposal environments, in, Sweden, 1997, pp. 94.
[41] Y. Li, J. Xu, Is niobium more corrosion-resistant than commercially pure titanium in fluoride-containing artificial saliva?, Electrochim. Acta, 233 (2017) 151-166.
[42] W. Wang, F. Mohammadi, A. Alfantazi, Corrosion behaviour of niobium in phosphate buffered saline solutions with different concentrations of bovine serum albumin, Corros. Sci., 57 (2012) 11-21.
[43] X. Yue, L. Zhang, Y. Hua, J. Wang, N. Dong, X. Li, S. Xu, A. Neville, Revealing the superior corrosion protection of the passive film on selective laser melted 316L SS in a phosphate-buffered saline solution, Appl. Surf. Sci., 529 (2020).
[44] Z. Duan, C. Man, C. Dong, Z. Cui, D. Kong, L. Wang, X. Wang, Pitting behavior of SLM 316L stainless steel exposed to chloride environments with different aggressiveness: Pitting mechanism induced by gas pores, Corros. Sci., 167 (2020).
[45] S. Fajardo, D.M. Bastidas, M. Criado, J.M. Bastidas, Electrochemical study on the corrosion behaviour of a new low-nickel stainless steel in carbonated alkaline solution in the presence of chlorides, Electrochim. Acta, 129 (2014) 160-170.
[46] G. Okamoto, Passive film of 18-8 stainless steel structure and its function, Corros. Sci., 13 (1973) 471-489.
[47] D.R. Lide, K.S. Lide, CRC handbook of chemistry and physics, (2001-2002).
[48] B. Zhang, J. Wang, B. Wu, X.W. Guo, Y.J. Wang, D. Chen, Y.C. Zhang, K. Du, E.E. Oguzie, X.L. Ma, Unmasking chloride attack on the passive film of metals, Nat. Commun., 9 (2018) 2559.
[49] Z. Cui, S. Chen, Y. Dou, S. Han, L. Wang, C. Man, X. Wang, S. Chen, Y. Cheng, X. Li, Passivation behavior and surface chemistry of 2507 super duplex stainless steel in artificial seawater: Influence of dissolved oxygen and pH, Corros. Sci., 150 (2019) 218-234.
[50] B. Hirschorn, M.E. Orazem, B. Tribollet, V. Vivier, I. Frateur, M. Musiani, Determination of effective capacitance and film thickness from constant-phase-element parameters, Electrochim. Acta, 55 (2010) 6218-6227.
[51] A. Kocijan, D.K. Merl, M. Jenko, The corrosion behaviour of austenitic and duplex stainless steels in artificial saliva with the addition of fluoride, Corros. Sci., 53 (2011) 776-783.
[52] D. Wallinder, J. Pan, C. Leygraf, A. Delblanc-Bauer, EIS and XPS study of surface modification of 316LVM stainless steel after passivation, Corros. Sci., 41 (1999) 275-289.
[53] F. Mansfeld, D.H. Hengstenberg, J.V. Kenkel, Galvanic corrosion of Al alloys I. effect of dissimilar metal, Corrosion-Us, 30 (1974) 343-353.
[54] Calculation of sputter etch rates.

[55] Z. Yan, L. Guo, Z. Li, Y. Yu, Q. He, Effects of laser glazing on CMAS corrosion behavior of Y2O3 stabilized ZrO2 thermal barrier coatings, Corros. Sci., 157 (2019) 450-461.
[56] M.H. Allahyarzadeh, M. Aliofkhazraei, A.R.S. Rouhaghdam, V. Torabinejad, Electrochemical tailoring of ternary Ni-W-Co(Al2O3) nanocomposite using pulse reverse technique, J. Alloys Compd., 705 (2017) 788-800.
[57] V. Torabinejad, M. Aliofkhazraei, A. Sabour Rouhaghdam, M.H. Allahyarzadeh, Ni–Fe–Mn–(nano)Al2O3 Coating with Modulated Composition and Grain Size, T. Indian I. Metals, 70 (2016) 1199-1207.
[58] V. Bonu, M. Jeevitha, V.P. Kumar, G. Srinivas, Siju, H.C. Barshilia, Solid particle erosion and corrosion resistance performance of nanolayered multilayered Ti/TiN and TiAl/TiAlN coatings deposited on Ti6Al4V substrates, Surf. Coat. Tech., 387 (2020).
[59] V. Torabinejad, M. Aliofkhazraei, A. Sabour Rouhaghdam, M.H. Allahyarzadeh, Corrosion properties of Ni-Fe-Cr (III) multilayer coating synthesized via pulse duty cycle variation, Mater. Corros., 68 (2017) 347-354.
[60] M. Urretabizkaya, C.D. Pallotta, N.D. Cristofaro, R.C. Salvarezza, A.J. Arvia, Changes in the composition of the passive layer and pitting corrosion of stainless steel in phosphate-borate buffer containing chloride ions, Electrochim. Acta, 33 (1988) 1645-1651.
[61] R.T. Loto, Pitting corrosion evaluation of austenitic stainless steel type 304 in acid chloride media, J. Mater. Environ. Sci., 4 (2013) 448-459.
[62] C.A. Apostolopoulos, S. Demis, V.G. Papadakis, Chloride-induced corrosion of steel reinforcement – mechanical performance and pit depth analysis, Constr. Build. Mater., 38 (2013) 139-146.
[63] D.D. Macdonald, The history of the point defect model for the passive state: a brief review of film growth aspects, Electrochim. Acta, 56 (2011) 1761-1772.
[64] C.L. Page, K.W.J. Treadaway, Aspects of the electrochemistry of steel in concrete, Nature, 297 (1982) 109-115.
[65] J. Ožbolt, G. Balabanić, G. Periškić, M. Kušter, Modelling the effect of damage on transport processes in concrete, Constr. Build. Mater., 24 (2010) 1638-1648.
[66] T. Li, J.R. Scully, G.S. Frankel, Localized corrosion: passive film breakdown vs. pit growth stability: part III. a unifyingset of principal parameters and criteria for pit stabilization and salt film formation, J. Electrochem. Soc., 165 (2018) C762-C770.